## Title

Structure of a Prokaryotic Sodium Channel Pore Reveals Essential Gating Elements and an Outer Ion Binding Site Common to Eukaryotic Channels



## Journal

Journal of Molecular Biology, 426(2)

## ISSN

0022-2836

## Authors

Shaya, David
Findeisen, Felix
Abderemane-Ali, Fayal
et al.

## Publication Date

2014

## DOI

10.1016/j.jmb.2013.10.010

Peer reviewed

Published in final edited form as:
*J Mol Biol*. 2014 January 23; 426(2): 467–483. doi:10.1016/j.jmb.2013.10.010.

# Structure of a prokaryotic sodium channel pore reveals essential gating elements and an outer ion binding site common to eukaryotic channels

**David Shaya**[1,*], **Felix Findeisen**[1,*], **Fayal Abderemane-Ali**[5,6,7], **Cristina Arrigoni**[1], **Stephanie Wong**[1], **Shailika Reddy Nurva**[1], **Gildas Loussouarn**[5,6,7], and **Daniel L. Minor Jr.**[1,2,3,4,†]

[1]Cardiovascular Research Institute, University of California, San Francisco, California 94158-9001

[2]Departments of Biochemistry and Biophysics, and Cellular and Molecular Pharmacology, University of California, San Francisco, California 94158-9001

[3]California Institute for Quantitative Biomedical Research, University of California, San Francisco, California 94158-9001

[4]Physical Biosciences Science Division, Lawrence Berkeley National Laboratory, Berkeley, CA 94720 USA

[5]Institut National de la Santé et de la Recherche Médicale, UMR1087, Nantes, France

[6]Centre National de la Recherche Scientifique, UMR 6291, Nantes, France

[7]l'institut du thorax, L'UNAM, Université de Nantes, Nantes, France

## Abstract

Voltage-gated sodium channels ($Na_V$s) are central elements of cellular excitation. Notwithstanding advances from recent bacterial $Na_V$ ($BacNa_V$) structures, key questions about gating and ion selectivity remain. Here, we present a closed conformation of $Na_V$Ae1p, a pore-only $BacNa_V$ derived from $Na_V$Ae1, a $BacNa_V$ from the arsenite oxidizer *Alkalilimnicola ehrlichei* found in Mono Lake, California, that provides insight into both fundamental properties. The structure reveals a pore domain in which the pore-lining S6 helix connects to a helical cytoplasmic tail.



†Correspondence: daniel.minor@ucsf.edu.
*These authors contributed equally



**Accession codes**

Crystallographic coordinates and structure factors are deposited with the PDB will be released immediately upon publication: 4LTO, $Na_V$Ae1p, crystal I, high calcium; 4LTP, $Na_V$Ae1p, crystal II, high calcium; 4LTQ, $Na_V$Ae1p, low calcium; 4LTR, $Na_V$Ae1p H245G, low calcium.

**Author contributions**

D.S, F.F., and D.L.M. conceived the study and designed the experiments. D.S., F.F., F.A.-A., S.W., and S.R. performed the experiments. D.S. S.W. and S.R. purified the proteins. D.S. grew the crystals and collected diffraction data. D.S. and F.F. solved and refined the structures and analyzed the data. F.F. F.A.-A., and C.A. designed and performed electrophysiological experiments and analyzed the data. G. L. and D.L.M. supervised the electrophysiology and analyzed data. D.L.M. analyzed data and provided guidance and support throughout. D.S., F.F., F.A.-A., C.A., G.L. and D.L.M. wrote the paper.

**Competing Interests**

The authors declare there are no competing interests.

Electrophysiological studies of full-length BacNa$_V$s show that two elements defined by the Na$_V$Ae1p structure, an S6 activation gate position and the cytoplasmic tail 'neck', are central to BacNa$_V$ gating. The structure also reveals the selectivity filter ion entry site, termed the 'outer ion' site. Comparison with mammalian voltage-gated calcium channel (Ca$_V$) selectivity filters, together with functional studies shows that this site forms a previously unknown determinant of Ca$_V$ high affinity calcium binding. Our findings underscore commonalities between BacNa$_V$s and eukaryotic voltage-gated channels and provide a framework for understanding gating and ion permeation in this superfamily.

## Introduction

Voltage-gated sodium channels (Na$_V$s) are large, multipass membrane proteins that are critical for cellular excitation[1; 2]. These channels are targets for drugs directed at neuropathic pain, migraine, arrhythmias, and epilepsy[3; 4], as well as environmental toxins[5]. Na$_V$s belong to the voltage-gated ion channel (VGIC) superfamily and are most closely related to voltage-gated calcium channels (Ca$_V$s)[6; 7]. Despite ion selectivity differences, mutational studies[8; 9; 10] and sequence similarities[6; 7] have suggested that Na$_V$s and Ca$_V$s share similar selectivity filter architectures[2]. However, details of this presumed commonality are unknown.

Discovery of a large family of bacterial Na$_V$s (BacNa$_V$s)[11; 12; 13] that may be ancestors of eukaryotic Na$_V$s and Ca$_V$s[14] has enabled delineation of structural principles shared by this VGIC superfamily branch. BacNa$_V$s are tetramers. Each subunit has six transmembrane segments that comprise a voltage-sensing domain (VSD) composed of the S1-S4 segments and a pore domain (PD) formed from the S5-S6 segments[15; 16; 17]. This subunit architecture is recapitulated in eukaryotic Na$_V$s and Ca$_V$s where four homologous six transmembrane repeats occur in a single polypeptide[2; 6; 7]. Protein dissection studies have demonstrated a further modular aspect of BacNa$_V$ architecture within the membrane domains. BacNa$_V$ 'pore-only' constructs lacking the VSD have been demonstrated to fol
d[18; 19; 20], assemble[18; 19; 20], and form functional, selective ion channels [19]. These demonstrations of BacNa$_V$ modularity are in accord wit

BacNa$_V$s have a conserved ~40 residue C-terminal cytoplasmic tail[28; 29] that is important for assembly [28] and function[29; 30]. However, this domain is either unresolved[15; 16] or absent from the crystallized constructs[17; 20] of prior BacNa$_V$ structures. Hence, its structure, relationship to the PD, and key functional elements have remained enigmatic.

Ion permeation is fundamental ion channel property[2]. Original descriptions of the BacNa$_V$ Na$_V$Ab suggested a single ion pore model[15]. In contrast, functional studies of Na$_V$s[2; 31] and Ca$_V$s[2; 32] support the presence of multi-ion pores as a means to affect ion selectivity and permeation[33; 34]. To date, only a single BacNa$_V$ ion binding site has been observed at the inner vestibule of the Na$_V$Rh selectivity filter[17]. Recent computational studies have suggested the possibility of other ion binding sites[35; 36], but the absence of experimental data have left unresolved questions regarding the existence of such sites, their exact locations, and residues involved in ion binding.

Here, we present the structure of Na$_V$Ae1p, a pore-only sodium channel derived from the *Alkalilimnicola ehrlichei* BacNa$_V$ Na$_V$Ae1[19]. The structure shows a closed conformation of a complete PD and cytoplasmic tail. Functional tests of key structural elements suggest that BacNa$_V$ opening involves changes at an S6 activation gate residue and a structural rearrangement in the neck region of the cytoplasmic tail. The structure also reveals an ion binding site in the selectivity filter that we term the 'outer ion' site. We demonstrate that the ion coordination residue comprising this site has a previously unrecognized counterpart in

mammalian $Ca_V$s that is crucial to high-affinity calcium binding, a result that lends support to long-standing proposals regarding the presence of multiple ion binding sites in $Ca_V$s[32; 33; 34]. Together, our results emphasize the deep evolutionary links between Bac$Na_V$s and mammalian channels and suggest that channels sharing this selectivity filter architecture have multiple ion binding sites.

## Results

### Structure of the pore-only channel $Na_V$Ae1p

We determined the structure of $Na_V$Ae1p, a 'pore-only' protein bearing the PD and cytoplasmic tail of the Bac$Na_V$ $Na_V$Ae1[19] (Supplementary Table S1) using X-ray diffraction data obtained from a I222 crystal that diffracted to a resolution of 4.00Å based on traditional measures such as $R_{pim}$ or Iσ/I. However, as it has been shown recently that adding weak high-resolution data beyond the commonly arbitrarily defined cutoffs used to judge resolution limits may be beneficial [37; 38; 39] we used data to a resolution of 3.46Å based on correlation coefficient (CC) evaluation ($CC1/_2$>0.1)[37] Molecular replacement using a PD ensemble from the *Acrobacter butzleri* ($Na_V$Ab)[15; 16] and *Rickettsia sp*. ($Na_V$Rh)[17] Bac$Na_V$s revealed electron density spanning from the beginning of the transmembrane segment S5 (Ile150) through the end of the cytoplasmic coiled-coil domain (Ser285) (Supplementary Figure S1A). $Na_V$Ae1p shows the funnel-shaped architecture found in other Bac$Na_V$s[15; 16; 17; 20] (Figure 1A, B). Each tetramer subunit is comprised of S5 and S6 transmembrane helices that form the outer and inner parts of the PD, respectively. The P1 and P2 pore helices bridge S5 and S6 and are connected by the selectivity filter (Figure 1).

Initial electron density maps (Supplementary Figure S1A) revealed an element absent from prior BacNaV structures, a long helical cytoplasmic tail (Figures 1A and 2A). The $Na_V$Ae1p tetramer forms the asymmetric unit and is packed in the crystal lattice such that the crystallographic axes are not coincident with the channel four-fold symmetry axis (Supplementary Figure S1B, Supplementary Table S1). This arrangement leads to four, independent but similar channel protomers arranged around the channel central axis in the asymmetric unit. Model building and refinement ($R_{work}/R_{free}$ 22.4 / 26.8, Table S1) showed that the pore-lining S6 helix continues for one turn after Met241, the intracellular pore constriction point (Figure 2A). A 40° bend at His245 follows and leads to a continuous helix that terminates with a four-stranded, parallel coiled-coil encompassing residues Leu265-Ser285 (Supplementary Table S2). The clear quality differences between electron density maps calculated using data resolution cutoffs based on traditional (Supplementary Figure S1C) versus $CC_{1/2}$ metrics (Supplementary Figure S1D) support the choice of resolution cutoff based on $CC_{1/2}$ values. The obvious differences in map quality reinforce the assertion that adherence to traditional metrics for defining resolution limits can result in the omission of useful diffraction data[37; 38]

The cytoplasmic tail is considerably longer than the pore-forming region (~65Å vs. ~40Å, respectively). Consequently, $Na_V$Ae1p spans ~110Å in the axial dimension and resembles the general architecture of a NaK-$Na_V$SulP chimera [29] and the full-length KcsA potassium channel[40] (Figure 2B and 2C, respectively). The coiled-coil is common among Bac$Na_V$s[28] and is thought to participate in channel assembly [28; 30]. Its location, C-terminal to a segment that trails S6, is reminiscent of similar domains from eukaryotic *K*v7 (KCNQ)[41; 42] and TRP channels [43] and agrees with predictions [28] and a similar structure in the NaK-$Na_V$SulP chimera[29] (Figure 2B).

The cytoplasmic tail arrangement resembles the stems of a flower bouquet. Individual helices interact extensively at the C-terminal base throughout the eighteen-residue coiled-coil but splay apart above Met267 into individual helical stems that connect the coiled-coil

to S6 (Figure 2D). This region, termed the 'neck' (Figures 1A and 2A), extends over six helical turns. The distance between the Cα positions and the superhelix axis widens from ~7Å in the coiled-coil to ~9Å in the neck (Figure 2D). The neck showed another unexpected feature, a large electron density that anomalous scattering indicated as a metal ion (Supplementary Figure S2A). B-factors indicate that the neck is as well ordered as other parts of the structure with the exception of the region near the neck ion (Supplementary Figure S2B).

Comparison of $Na_VAe1p$ with a chimera between the nonselective NaK channel and the BacNaV $Na_VSulP$ coiled-coil[29] shows good agreement in the coiled-coils (Figure 2B and E, Table S3) (RMSD Cα = 1.2 Å for the tetramer). Contrastingly, the corresponding KcsA region, where there is no superhelical coil (Supplementary Table S2), poorly matches the $Na_VAe1p$ coiled-coil (Figure 2C and 2F, Supplementary Table S3) and reveals an unexpected diversity in how seemingly similar cytoplasmic domains can assemble. The essentially continuous helical conformation from S6 to the coiled-coil is contrary to predictions from circular dichroism and sequence analysis suggesting that this $BacNa_V$ region is disordered[28]. Notably, the neck has an abundance of charged and polar residues (15/20 residues) (Figures 1C and 2G). This density of hydrophilic residues may be important for neck function.

## Comparison of $Na_VAe1p$ pore region with other $BacNa_V$ structures

$Na_VAe1p$ conforms to expectations for a closed conformation as the selectivity filter is not collapsed and the intracellular gate is closed (Figure 3A–B, Figure S2C). Overall, the PD superposes well with other $BacNa_V$s (Figure 3C, Table S3). Despite the VSD absence, S5 has position similar to that seen in $Na_VAb$ and is only substantially different than S5 of $Na_VRh$, which is the outlier of currently known $BacNa_V$ structures. The main variations from other $BacNa_V$s lie in the C-terminal ends of S6 from the putative inactivated $Na_VAb$ conformation[16] and $Na_VMs$ pore[20] (Figure 3C, and Figure S3).

$Na_VAe1p$ has a wide extracellular funnel that connects through the selectivity filter to the central cavity (Figure 3A). Side chain oxygens of selectivity filter residue Ser198 form the narrowest extracellular constriction (pore radius, 1.6Å) (Figure 3B). This is larger than that seen at the analogous $Na_VRh$ position (pore radius, 1.1Å), where the filter is closed[17], but is not as wide as in $Na_VAb$ (pore radius, 2.3Å)[15] (Figure 3B, Figure S4). It is important to point out that the structure of $Na_VMs$ has a diameter that is close to that of the other $BacNa_V$s (Figure 3B) due the similarity of its backbone positions with the other $BacNa_V$ structures (Supplementary Table S3). The remaining differences for $Na_VMs$ are largely due to the fact that the $Na_VMs$ structure has incomplete sidechains at seven out of eight of the positions that correspond to the $Na_VAe1p$ residues that constrict the inner cavity, Phe233 and Ile 237 (Figure 3A), and truncates in three of the subunits before the portion that corresponds to $Na_VAe1p$ Met241. The inner diameter of all of the solved structures contrasts to that of the open state model $Na_VMs_{OM}$ that is generated from the most deviant subunit in the $Na_VMs$ structure (Figure 3B)[20].

The inside of the selectivity filter abuts an aqueous cavity that includes lateral openings to the membrane and that ends in a constriction formed by S6 residues Phe223, Ile237, and Met241 (Figure 3A–B), positions largely conserved among $BacNa_V$s (Figure 1C). Both the presence of Fo-Fc electron density (Figure 3D) and a sidechain sulfur difference anomalous signal (Supplementary Figure S2A) support the placement of Met241 as the site of intracellular pore closure. This position corresponds to the suggested $Na_VAb$ activation gate[15] and strikingly, forms a closure point further along S6 than in all but the initial $Na_VAb$ structure (Figure 2B). It is notable that evaluation of possible boundaries of the lipid bilayer hydrophobic portion[44] suggests that unlike other $BacNa_V$ structures, the $Na_VAe1p$ activation

gate region protrudes from the bilayer core into the zone comprising phospholipid head groups (Supplementary Figure S5).

## Identification of the 'outer ion' binding site

We found a large positive electron density peak perched on the four-fold axis of the channel at the selectivity filter outer mouth (Figure 3E). Calculation of anomalous difference maps at 6.5Å revealed a strong peak (11a) indicating the presence of a non-protein anomalous scatterer (Figure 3F, Supplementary Figure S6A–S6D). Recognizing there could be challenges in identifying this peak due to the data resolution, we searched for other evidence that it represented an ion and not noise or some other possibility. We found a similar non-protein anomalous scatterer at the exact same location in a second lower resolution (3.80Å) data set ($Na_VAe1p$, Crystal II, Supplementary Table S1, Supplementary Figure S6C) obtained from a crystal grown using the same high calcium (200 mM $CaCl_2$) conditions as the crystal that yielded the 3.46Å resolution data set. By contrast, there was no anomalous peak at this location in maps calculated from crystals grown without calcium (Supplementary Figure S1E and S6C). In all three cases, the maps, which are all calculated at the same resolution (6.5Å), showed strong evidence for the neck ion. Finally, structural studies of the H245G mutant, in which crystals were grown in the absence of calcium and in the identical spacegroup as $Na_VAe1p$ Crystal I and Crystal II (Supplementary Figure S6C), gave no evidence for the selectivity filter ion. Given these multiple lines of evidence that the anomalous peak at the selectivity filter outer mouth depends on the presence of calcium, we assigned this density as a calcium ion.

Inclusion of the ion alone in the refinement left substantial unaccounted electron density. Taking into account the ion position and likelihood that it is partly solvated, we modeled four waters using standard calcium coordination geometry (Figure 3E). We also found additional positive difference ($F_O$-$F_C$) electron density extending from the outer ion position through the selectivity filter along the four-fold channel axis; however, we were unable to model whether this arises from ions or solvent (Supplementary Figure S6E). The refined structure shows a partially hydrated calcium ion coordinated by four $Na_VAe1p$ serine oxygens and four water molecules, giving a coordination number common to protein-$Ca^{2+}$ complexes[45] and serine oxygen-$Ca^{2+}$ distances (2.9Å −3.5Å) that are within those for calcium ions partially coordinated by protein ligands[45; 46]

We denote the calcium ion position as the 'outer ion' because it is separated from the previously reported selectivity filter inner ion position[17; 35] by 10.7Å (Figure 3C). The outer ion site also does not correspond to the position of the unassigned selectivity filter density reported for $Na_VMs$[20]. Observation of the outer ion binding site, together with the strong structural (Figure 3C) and sequence similarity (Figure 1C) of the region and previous identification of an inner ion site establishes that $BacNa_V$ selectivity filters have more than one ion binding site. Sodium and calcium ions have similar radii (0.95Å vs. 0.99Å, respectively) and coordination geometries[2]. Hence, the outer ion position appears to mark the site of entry and partial dehydration as the ion passes into the selectivity filter.

To facilitate comparison among $Na_V$, $Ca_V$, and $BacNa_V$ selectivity filters, we denote the residue corresponding to the mammalian $Na_V$ 'DEKA' motif[2] and the conserved glutamates in $Ca_V$s[2; 33] and $BacNa_V$s (Figure 1C) as position '0'. Other residues are numbered positively or negatively relative to this residue (Figure 4A). Hence, the $Na_VAe1p$ Ser198 (+1) sidechain oxygens coordinate the outer ion (Figure 3E). Comparison of $BacNa_V$ and $Ca_V$ selectivity filter sequences revealed that the (+1) position is strictly conserved as an acidic residue in $Ca_V$ domain II selectivity filters (Figure 4B). This (+1) position had not been previously implicated in $Ca_V$ selectivity. As it plays a role in $BacNa_V$ calcium

selectivity[19; 47], the compelling similarities together with the observation of a bound calcium ion prompted us to examine the role of the (+1) position in a mammalian $Ca_V$.

### Outer ion site is important for mammalian $Ca_V$ ion binding

Calcium selectivity in $Ca_V$s is thought to arise from the interaction of permeant calcium ions with a ring of selectivity filter (0) position glutamates[33; 48]. Following experiments that first demonstrated the importance of the (0) position glutamates[33], we used two-electrode voltage clamp to measure calcium block of lithium currents through human cardiac $Ca_V1.2$ channels expressed in *Xenopus* oocytes and examined how (+1) position mutations in domain II affect the high affinity calcium site. In contrast to previous reports[33], we found that D707N channels exhibited a reduction in the apparent calcium affinity relative to wild type ($IC_50$ 11.3 ± 2.0 μM, and 1.9 ± 0.2μM, D707N and wild-type, respectively) (Figure 4C–D). This change was equivalent to that caused by the charge neutralization E1115Q ($IC_{50}$ 15.1 ± 1.9 μM), the (0) position glutamate neutralization having the largest reported impact on the high affinity site[33; 48] Changing D707 to alanine to mimic the corresponding $Ca_V$ domain IV position caused a reduction in apparent affinity similar to D707N (IC50 13.6 ± 2.1 μM). Complete removal of the D707 sidechain by D707G to mimic the equivalent position of $Ca_V$ domains I and III caused an even greater reduction in calcium binding (IC50 22.8 ± 6.7 μM). The magnitude of the effects of the D707 neutralizations are striking as this position is much more exposed to bulk solvent than the (0) position glutamate and strongly suggest that the effects of the D707 mutation are through direct interaction with $Ca^{2+}$ rather than a indirect consequence of electrostatic environment alteration. These data demonstrate the importance of a previously unrecognized calcium binding determinant of mammalian $Ca_V$s. These findings underscore the similarities between selectivity filters of homomeric $BacNa_V$s and their more distant eukaryotic relatives, which have four non-identical selectivity filter repeats.

### S6 activation gate residue and neck are important for $BacNa_V$ gating

Observation of a complete $BacNa_V$ cytoplasmic domain connected to a closed pore prompted us to test how the newly described channel elements (Figure 5A) contribute to function. In line with the low success rate of $BacNa_V$ functional expression[12; 17], our initial attempts to measure currents from full-length $Na_VAe1$ using transfected mammalian cells or mRNA injected *Xenopus* oocytes failed. Therefore, we turned to $Na_VSp1$, a previously characterized *Silicibacter pomeroyi* homolog[12] (Figure 1C and Figure 5B).

As prior structural studies have not achieved consensus regarding which S6 residues close the intracellular side of the pore (Figure 3B), we first examined the $Na_VSp1$ S6 positions equivalent to those that narrow the $Na_VAe1p$ intracellular side (Figure 3A). Alanine substitution in each of the two helical turns above the constriction site, $Na_VAe1p$ F233 and I237 ($Na_VSp1$ L212A and I216A) (Figure 3A and Figure 5A, Supplementary Figure S7A), did not affect the voltage-dependence of activation ($V_{1/2,act}$) ($\Delta V_{1/2,act}$ = −1.0 ± 4.5 and −0.4 ± 4.8 mV, respectively) (Figure 5C, Table 1). However, these mutants did shift the voltage-dependence of inactivation ($V_{1/2,inact}$) to more negative potentials ($\Delta V_{1/2,inact}$ = −14.8 ± 4.3 and −14.0 ± 3.8 mV, respectively) (Figure 5C, Table 1), decreased the inactivation time constants, and accelerated recovery from inactivation (Supplementary Figure S7B and S7C). By contrast, alanine substitution of the position equivalent to the pore occlusion point, $Na_VAe1p$ Met241 ($Na_VSp1$, M220A) (Figure 3A and Figure 5A) caused dramatic negative shifts in both $V_{1/2,act}$ and $V_{1/2,inact}$ ($\Delta V_{1/2,act}$ = −49.8 ± 3.3 mV and $\Delta V_{1/2,inact}$ = −40.0 ± 3.5 mV)(Figure 5D, Table 1), but left the inactivation time constants and recovery from inactivation unaltered (Supplementary Figure S7B–C). The major effect of $Na_VSp1$ M220A on $V_{1/2,act}$ contrasted against the absence of $V_{1/2,act}$ changes from mutation of residues further into the central cavity suggests a critical role for this position in stabilizing the closed

state of the channel and indicates that the more distal positions are important for inactivation only.

Because of its direct structural connection to the activation gate, we next examined how the helical structure of the neck affected channel behavior by using a strategy of glycine substitutions to destabilize the helical conformation[49; 50; 51]. Because $BacNa_V$ necks have variable lengths, we focused on the most conserved region (Figure 1C). Similar to the S6 mutant $Na_VSp1$ M220A, single glycine substitutions at each of the three residues below the bend $Na_VAe1p$ Ala248, Glu249, Asp250 ($Na_VSp1$, A226G, E227G, and D228G) caused a significant negative shift in $V_{1/2,act}$ (Figure 5E, Table 1, Figure S7D–E). By contrast, alanine substitutions at $Na_VSp1$ E227 and D228 yielded essentially wild-type channels (Figure 5E, Table 1, Supplementary Figure S7D–E), indicating that the glycine impact comes from increased flexibility rather than sidechain deletion. Increasing the consecutive numbers of $Na_VSp1$ neck glycines to two (residues 227–228), three (residues 226–228), and seven (residues 226–232) further facilitated activation gate opening that was coupled to negative shifts in $V_{1/2}$,inact ($\Delta V_{1/2,act}$ = −25.3 ± 2.6, −35.0 ± 3.8, and −40.7 ± 3.9 mV and $\Delta V_{1/2,inact}$ = −4.5 ± 3.2, −18.1 ± 3.6 and −22.1 ± 5.2 mV, for 2Gly, 3Gly and 7Gly, respectively) (Figure 5E and F, Table 1). The 2Ala mutant revealed that part of the shift caused by the 2Gly mutant arises from a synergistic effect of removing $Na_VSp1$ E227 and D228 simultaneously ($\Delta V_{1/2,act}$ = −15.7 ± 3.4 versus −25.3 ± 2.6 mV, for 2Ala and 2Gly, respectively (Figure 5E, Table 1) that indicates an additional role for these charges. Nevertheless, the 7Ala mutant had activation properties similar to wild-type and that strongly contrasted the large negative shifts in $V_{1/,act}$ and $V_{1/2,inact}$ caused by 7Gly ($\Delta V_{1/2,act}$ = 4.7 ± 4.4 versus −40.7 ± 3.9 mV for 7Ala and 7Gly, respectively). The major negative shifts in $V_{1/2,act}$ produced by neck substitutions that are detrimental to helix formation strongly supports the idea that a structured neck is critical for closed state stabilization.

The majority of neck mutants causing negative shifts in $V_{1/2,act}$ also elicited negative shifts in $V_{1/2,inact}$ (Figure 5E, Table 1). However, unlike previously reported mutations in the $Na_VSulP$ coiled-coil that slowed $\tau_{inact}$ by an order of magnitude or more[29] most of the neck mutants left $\tau_{inact}$ unperturbed (Supplementary Figure S7F–G). Of the few that did not (E227G, D228G, 2G, 7G, P< 0.001), none caused a perturbation larger than a factor of three. To examine this discrepancy further, we characterized $Na_VSp1$ R242E (Supplementary Figure S8), a substitution at a conserved position at the N-terminal end of the coiled-coil region that was reported cause a negative shift in $V_{1/2,act}$ and slow $Na_VSulP$ inactivation by ~37-fold[29]. Although $Na_VSp1$ R242E did cause a negative shift in $V_{1/2,act}$ (Table 1), unlike its $Na_VSulP$ counterpart, this change caused only a modest (~2.7-fold, P = 0.04) slowing of inactivation (Supplementary Figure S8D).

Finally, we tested the consequences of alanine and glycine substitutions at the bend, $Na_VAe1p$ His245 ($Na_VSp1$, H224) (Figure 5G, Supplementary Figure S9A). $Na_VSp1$ H224A did not affect $V_{1/2,act}$ or $V_{1/2,inact}$ ($\Delta V_{1/2,act}$ = 2.8 ± 4.2, $\Delta V_{1/2,inact}$ = −5.4 ± 4.8 mV) (Figure 5G, Table 1), but did slow inactivation (~2-fold, P< 0.001) (Supplementary Figure S9B). In contrast, $Na_VSp1$ H224G spared $V_{1/2,act}$ and caused a large negative shift in $V_{1/2,inact}$ ($\Delta V_{1/2,act}$ = −4.5 ± 3.9 mV, $\Delta V_{1/2,inact}$ = −25.0 ± 4.0 mV) (Figure 5G, Table 1). Although local disorder (Supplementary Figure S2B) precluded us from modeling the $Na_VAe1p$ His245 sidechain, this residue could co-ordinate the neck ion. To test the structural consequence of loss of this potential ligand, we determined a 5.8Å resolution structure of $Na_VAe1p$ H245G crystallized from a low calcium condition (Supplementary Table S1). The structure showed no major changes from wild-type except for the loss of anomalous density for the neck ion and outer ion (Supplementary Figure S8C)(RMSD Cα = 0.5 Å for the tetramer relative to wild-type). Hence, the bend residue appears to be important

for neck ion coordination but the neck ion is not essential for the bend structure or helical character of the neck.

Our structure-based mutational studies uncovered two functional phenotypes. Mutations in the activation gate and neck having negative shifts in $V_{1/2,act} \geq -20$ mV also caused negative shifts in $V_{1/2,inact}$, suggesting that the two processes are strongly coupled. Mutations at S6 residues above the activation gate and bend residue H224, selectively impacted $V_{1/2,inact}$ (Table 1). Together, these data support the ideas that (i) the $Na_VAe1p$ structure represents a closed state, (ii) destabilization of the neck facilitates channel opening, and (iii) residues in S6 above the constriction site and at the bend are important for the molecular transitions underlying inactivation.

### Neck destabilization allows $Na_VAe1$functional characterization

Having established the importance of the neck helical structure for closed state stabilization, we revisited $Na_VAe1$ functional studies to test whether glycine substitution in the neck would permit us to record from full-length channels. Indeed, $Na_VAe1$ channels bearing the 3Gly mutation (residues 248–250) produced voltage-dependent channels (Figure 6A–B). These had a $V_{1/2,act}$ similar to $Na_VSp1$ but ~40 mV more positive than the equivalent $Na_VSp1$ 3Gly mutant ($V_{1/2,act}$ = 32.1 ± 2.8, 27.4 ± 1.1, and −7.6 ± 2.1 mV for $Na_VAe1$ 3Gly, $Na_VSp1$, and $Na_VSp1$ 3Gly, respectively). These results further support the idea that the neck helical structure is important for closed state stabilization and suggest that wild-type $Na_VAe1$ has a very positive $V_{1/2,act}$ of activation that had prevented functional characterization.

The ability to record from $Na_VAe1$ 3Gly allowed us to test the functional properties of the $Na_VAe1$ selectivity filter defined by our structure. In agreement with the strong selectivity filter conservation (Figure 1C), biionic recording experiments (Figure 6C–D) showed that $Na_VAe1$ has selectivity properties similar to other $BacNa_Vs$ including $Na_VSp1p$[19], the ‘pore-only’ version of $Na_VSp1$ ($P_{Ca}/P_{Na}$ = 0.07 ± 0.02 and 0.08 ± 0.01, for $Na_VAe1$ 3Gly and $Na_VSp1p$, respectively), and $Na_VBh1$ (NachBac)[46]. Due the relatively low current amplitude of $Na_VAe1$ 3Gly, we were restricted to this extrapolation method of examining the permeability ratio. Hence, we validated the measurement by determining the ion selectivity of full-length $Na_VSp1$ 3Gly, which expresses much better than $Na_VAe1$ 3Gly, by two methods, the extrapolation method used to examine $Na_VAe1$ 3Gly and a tail current protocol (Supplementary Figure S10). Both methods gave the same $P_{Ca}/P_{Na}$ ratio (0.05 ± 0.02 and 0.07 ± 0.02, respectively) and agree with the values for $Na_VAe1$ 3Gly and the ‘pore only’ $Na_VSp1p$. These results support the idea that the 3Gly mutation has minimal influence on selectivity and that $Na_VAe1$ is a sodium selective channel.

## Discussion

Structure determination of the ‘pore-only’ $BacNa_V$ $Na_VAe1p$ revealed previously uncharacterized $BacNa_V$ architectural features that are important for function. The presence of the long, helical intracellular domain allowed the complete definition of S6, which extends into the intracellular side of the membrane (Supplementary Figure S5). Relative to all but the initial $Na_VAb$ structure[15], which contained pore-lining cysteine mutants near the activation gate that may have influenced S6 positioning, this structure places the intracellular gate more towards the S6 C-terminus (Figure 3B). It seems likely that the absence of a consensus among the prior $BacNa_V$ structures in defining the site of this important channel element arises from the fact that they lack the intracellular domain. The structural plasticity of the intracellular gate seems a likely consequence of it being the central point of structural changes required for gating and inactivation. Our observations are not unlike those described for KcsA in which the full-length structure[40] showed that the

activation gate closure point was more intracellular than defined from a structure lacking the intracellular domain[52]. The $Na_VAe1p$ activation gate and subsequent helical extension of S6 should protrude beyond the boundaries of the hydrophobic portion of the lipid bilayer into the lipid headgroups (Supplementary Figure S5). This location may have important consequences as, based on voltage-gated potassium channel studies [26], it could allow the C-terminal portion of S6 to interact directly with the phospholipid headgroups in a way that could influence function. It might also permit interactions with the proposed S4-S5 linker closed state pose[26].

Our studies demonstrate that destabilizing the helical structure of the neck causes negative shifts in $V_{1/2,act}$. The largest perturbation, 7Gly in which two full helical turns of the neck are glycines, has effects that are of the same magnitude as activation gate disruption (Table 1). In both cases, there are parallel shifts in $V_{1/2,inact}$ that indicate that activation and inactivation are tightly coupled. Previous work with $Na_VSulP$ showed that coiled-coil disruption slowed inactivation kinetics by more than an order of magnitude, suggesting that this structure as a role in accelerating inactivation[29]. Unlike these effects, which were caused by disruption further from the pore, destabilization of the $Na_VSp1$ neck had minimal impact on inactivation time constants (Supplementary Figure S7F–G). Moreover, examination of a coiled-coil mutation, R242E, equivalent to one from $Na_VSulP$ that caused a dramatic slowing of inactivation, negatively shifted $V_{1/2,act}$ but failed to produce a similar effect on $Na_VSp1$ inactivation kinetics (Figure S8D). Thus, the major role of the neck is to stabilize the channel closed state.

Our studies lead us to propose the following model for $BacNa_V$ gating (Figure 7). In the closed state, represented by the $Na_VAe1p$ structure (Figure 1), the intracellular side of the channel central pore is occluded by the activation gate residue constriction ($Na_VAe1p$ M241). Opening would proceed with a radial expansion of this region[15] accompanied by an order→disorder transition in the neck. The neck region is a site of potential disorder[28] The abundance of polar and charged neck residues (Figure 2G) may aid the transition to this state and assist in permeant ion escape into the cytoplasm (Figure 7). Whether such a state resembles the proposed $BacNa_V$ open state model[20] is unclear, as much of the end of S6, including the activation gate equivalent of $Na_VAe1p$ Met241 is absent from the $Na_VMs$ structure. Eukaryotic $Na_V$s and $Ca_V$s lack an equivalent of the C-terminal tail; however, the prevalence of similarly located C-terminal coiled-coil domains among diverse eukaryotic VGICs[41; 42; 43] and the importance of the intervening region that connects S6 to the coiled-coils for channel regulation by a diverse factors[53; 54] suggests that the essence of this proposed $BacNa_V$ mechanism has parallels in eukaryotic VGICs.

The ionic radii and coordination geometries of sodium and calcium ions are similar [2]. Hence, the $Na_VAe1p$ outer ion position, reveale*d* by calcium, appears to mark the site of entry and partial dehydration as the permeant ion interacts with the (+1) residues and passes into the selectivity filter. This role in ion coordination agrees with the observation that a single S^D change at the NaChBac ($Na_VBh1$) (+1) position alters selectivity for calcium over sodium by ~200 fold[47] and with simulations suggesting that residues forming the outer ion site may be involved in ion recruitment[35]. The outer ion site may also participate in the divalent ion block described for NaChBac (NaVBh1)[11; 17] and the NaChBac/$Na_VRh$ selectivity filter chimera[17] as it corresponds well with the predicted ‘site 1’ blocking site from molecular dynamics simulations [35] It is also striking that structural changes at the (+1) serine cause substantial alterations to the size of the selectivity filter entrance in the putative inactivated conformation of $Na_VAb$[16] and in $Na_VRh$, where the (+1) serine occludes the pore (Figure S4). Thus, this outer ion site may not only be important for engagement of permeant and blocking ions but may participate in rearrangements leading to slow inactivation[55]

Observation of an outer ion binding site in the selectivity filter together with the prior discovery of a selectivity filter inner ion site [17] (Figure 3C) and strong sequence and structural conservation of this region (Figure 1C and Figure 3C) shows that $BacNa_V$ selectivity filters posses more than one ion binding site. It seems possible, especially given the ~10Å separation between outer and inner ion sites, that multiple ions may occupy the selectivity filter simultaneously. This situation would be tantalizingly close to accepted ideas regarding multi-ion pores in mammalian $Na_V$ and $Ca_V$ counterparts[2; 31; 32; 34], not unlike that of potassium channels[56], in line with recent computational studies of $BacNa_V$ filters[57], and argues against the single ion pore model suggested in the initial $BacNa_V$ structure analysis[15].

Identification of the outer ion binding site uncovered a previously unknown role for the analogous conserved (+1) position in mammalian $Ca_V$s as an important determinant for calcium selectivity. Notably, despite its more exposed location, the impact of neutralization of the (+1) position is equivalent to that of neutralization of the (0) position glutamate that resides deeper in the selectivity filter (Figure 4D), strongly suggesting that it may interact directly with the permeant ion. These results demonstrate a deep commonality between $BacNa_V$s and eukaryotic voltage-gated channels that should facilitate understanding ion permeation and gating in the superfamily.

## Materials and methods

### Crystallization

$Na_V$Ae1p was expressed and purified in β-dodecyl maltoside (DDM) as described [19]. For high calcium-condition crystals, purified protein was concentrated to 15 mg $ml^{-1}$ by centrifugal filtration (Amicon® Ultra-15 100-kDa MW cutoff, Millipore) and mixed with 5M trimethylamine oxide (TMAO[58; 59]) creating a solution of 13.5 mg $ml^{-1}$ protein, 0.25 mM DDM, 0.5M TMAO, 200 mM NaCl, 20 mM Na-HEPES, pH8.0. The protein was crystallized using hanging-drop vapor diffusion at 4°C over a reservoir of 200 mM $CaCl_2$, 30% PEG 400, 100 mM Na-acetate, pH 5.0. 0.7 μl of protein-TMAO solution was laid on a 0.7 μl drop of mother liquor that had been mixed with agarose to a final concentration of 0.25% and left to solidify at room temperature for 1 min. I222 crystals grew from precipitate to a final size of ~200× 70 x 15 μm after three weeks.

For low calcium condition crystals, protein was concentrated to 13.5 mg $ml^{-1}$ (Amicon® Ultra-15 100-kDa MW cutoff, Millipore) following exchange into 0.25 mM DDM, 200 mM NaCl, 20 mM Na-HEPES, pH 8.0, during the last size exclusion chromatography purification step. $P4_2$ crystals were grown by hanging drop vapor diffusion at 4°C from equal volumes of protein reservoir solution of 200 mM $MgCl_2$, 30% polyethylene glycol (PEG) 400, 100 mM MES, pH 6.5. Crystals appeared in 2 days, grew to ~200 × 50 x 50 μm in ~two weeks.

$Na_V$Ae1p H245G was expressed and was purified as $Na_V$Ae1p [19] using a final size-exclusion chromatography buffer of 0.3 mM DDM, 200 mM NaCl, 2mM $MgCl_2$, 20 mM Na-HEPES, pH 8.0. Purified protein was concentrated to 13.5 mg $ml^{-1}$ (Amicon® Ultra-15 100-kDa MW cutoff, Millipore). 1 μl hanging drops were set-up at 4°C using a 24 well VDX Plate™ (Hampton Research) over a reservoir of 28% PEG 400, 100 mM Na acetate, pH 4.5. I222 crystals grew overnight and reached maximal proportions of ~300 × 75 X 15 μm after two weeks.

### Data collection, structure determination and refinement

Crystals were frozen directly into liquid $N_2$ for data collection. Diffraction data were collected at Advanced Light Source Beamline 8.3.1, Lawrence Berkeley National

Laboratory, integrated with MOSFLM 7.0.4[60] and scaled with SCALA (3.3.20)[61]. Phase information was obtained by molecular replacement with an ensemble model based on the 3RVY, 4DXW, and 4EKW pore domains using Phaser (2.1.4)[62]. Model was improved using cycles of manual rebuilding, Coot (0.7) [63], and refinement, Refmac (5.7.32)[64]. NCS-averaged maps improved apparent electron density and allowed placing of most of the side chains. For the high calcium structure, initial tight NCS restraints were employed and later relaxed for all segments except for residues 183– 208 and 214–220. For both the low calcium structure and the $Na_VAe1p$ H245G mutant tight NCS restraints were employed throughout.

## Two electrode voltage-clamp electrophysiology

Human $Ca_V1.2$ ($\alpha_1$C77, GenBank CAA84346), rat $Ca_V\beta_{2a}$ (GenBank NP 446303), and $Ca_V\alpha_2\delta$-1(GenBank NM_00182276) were used for two-electrode voltage clamp experiments in *Xenopus* oocytes. Mutations were introduced using Quikchange (Stratagene). Linearized cDNA was translated into capped mRNA using the T7 mMessenger kit (Ambion). 50 nl of $Ca_V1.2\alpha_1$, $Ca_V\beta_{2a}$, and $Ca_V\alpha_2\delta$-1 mRNA at a 1:1:1 molar ratio were injected into *Xenopus* oocytes. Two-electrode voltage-clamp experiments were performed 2 to 3 days post-injection. Oocytes were injected with 50 nl of 100 mM BAPTA 4' before recording to minimize calcium-activated chloride currents. Recording solutions contained 100mM LiOH, $Ca(NO_3)_2$ at the concentration indicated, and 10 mM HEPES, adjusted to pH 7.4 using $HNO_3$. $Ca^{2+}$ concentrations were verified using a $Ca^{2+}$ electrode. The solution with a nominal free Ca2+ concentration of 3nM contained 170 μM $Ca(NO_3)2$ and 15 mM EGTA. Buffered solutions with nominal free $Ca^{2+}$ concentrations of 100nM, 300 nM, and 1 μM were also tested and gave results similar to the corresponding solutions in which $Ca^{2+}$ was not buffered by EGTA. Electrodes were filled with 3M KCl and had resistances of 0.3–1.0 MΩ. Recordings were conducted at room temperature from a holding potential of −90 mV. Leak currents were subtracted using a P/4 protocol. Currents were analyzed with Clampfit 8.2 (Axon Instruments). All results are from at least two independent oocyte batches. Dose-response curves were calculated as follows: $Ix/I_{3nMCa} = 1/(1+x/IC_{50})$, where $I_x$ is current at the $Ca^{2+}$ concentration x and IC50 is the half-maximal inhibitory concentration.

## Patch-Clamp electrophysiology

BacNaVs from *Silicibacter pomeroyi*, NavSp1, and *Alkalilimnicola ehrlichei*, $Na_VAe1$, were cloned into the pIRES2-EGFP vector (Clontech, Mountain View, CA). All the $Na_VSp1$ mutants were made using the QuikChange® Site-Directed Mutagenesis Kit (Stratagene, La Jolla, USA) and sequenced before recordings. Human embryonic kidney cells (HEK 293) were grown at 37 °C under 5% $CO_2$, in a Dulbecco's modified Eagle's medium (DMEM) supplemented with 10% fetal bovine serum, 10% L-glutamine and antibiotics (100 IU/ml penicillin and 100 mg/ml streptomycin), (UCSF Cell Culture Facility). HEK 293 cells were transfected (in 35 mm diameter wells) with LipofectAMINE™ 2000 (Invitrogen, Carlsbad, CA, USA and plated onto coverslips coated with Matrigel (BD Biosciences, San Diego, CA, USA). 2 μg of DNA was used except for the L212A and I216A for which 4 μg of DNA was used to increase current amplitude.

Transfected cells were identified visually enhanced green fluorescent protein (EGFP) expression. Whole cell patch-clamp [65] was used to record $Na^+$ current at room temperature (23 ± 2 °C) 48–72 h post-transfection. Acquisition and analysis were performed using pCLAMP 9 (Molecular Devices, Sunnyvale, CA, USA) and an Axopatch 200B amplifier (Molecular Devices, Sunnyvale, CA, USA). Pipettes were pulled from borosilicate glass capillaries (TW150F-3, WPI, Sarasota, USA) and polished (MF-900 microforge, Narishige, Tokyo, Japan) to obtain 2–3 MΩ resistances. Sixty to eighty percent of the voltage error due

to the series resistance was compensated. Unless stated otherwise, pipette solution contained, in mM: 120 Cs-methane sulfonate, 8 NaCl, 10 EGTA, 2 Mg-ATP, and 20 HEPES (pH 7.4 with CsOH). Bath solution contained, in mM: 155 NaCl, 1 CaCl2, 1 $MgCl_2$, 5 KCl, 10 HEPES, and 10 glucose (pH 7.4 with NaOH).

For reversal potential measurements to determine the $Na^+$ and $Ca^{2+}$ relative permeabilities, pipette solution contained, in mM: 100 Na-Gluconate, 10 NaCl, 10 EGTA, 20 HEPES (pH 7.4 adjusted with NaOH, [Na] total 130). For tail protocol experiments on $Na_V$Sp1 3Gly the pipette solution contained in mM: 30 Na-Gluconate, 10 NaCl, 10 EGTA, 20 HEPES, 70 NMDG-Cl (pH 7.4 adjusted with NaOH, [Na] total 45). External solution in both was, in mM: 5 NMDG-Cl, 100 CaCl2, 20 HEPES (pH 7.4 adjusted with CaOH, [Ca] total 107.5). The permeability ratio of $Ca^{2+}$ over $Na^+$ was estimated using the following equation:

$$P_{Ca}/P_{Na}=a_{Na,int}[\exp(E_{rev}F/RT)][\exp(E_{rev}F/RT)+1]/(4a_{Ca\ ext}),$$

where R, T, F, and $E_{rev}$ are the gas constant, absolute temperature, Faraday constant, and reversal potential, respectively (int, internal; ext, external)[2] $Ca^{2+}$ and $Na^+$ activity coefficients were estimated as follows:

$$a_s=\gamma_s[X_s],$$

where activity, $a_s$, is the effective concentration of an ion in solution, s related to the nominal concentration $[X_s]$ by the activity coefficient $\gamma_s$. $\gamma_s$ was calculated from the Davies equation. The calculated activity coefficients were $\gamma_{(Na)int}$ = 0.76 and $\gamma_{(Ca)ext}$ = 0.33. The liquid junction potentials were calculated by the JPCalc program (P. Barry) within Clampex (Molecular Devices) and taken into account to determine $E_{rev}$.

## Supplementary Material

Refer to Web version on PubMed Central for supplementary material.

## Acknowledgments

We thank Christine Rumpf for expert molecular biology assistance and J. Holton and G. Meigs at ALS 8.3.1 for data collection assistance. We thank K. Brejc, L. Jan, and E. Reuveny for helpful manuscript comments, and Minor lab members for support throughout these studies. This work was supported by grants to D.L.M. from NIH R01-HL080050, R01-DC007664, and U54-GM094625 and the American Heart Association 0740019N, an American Heart Association Postdoctoral Fellowship to D.S., and Fulbright Scholarship and a Monahan Foundation Fellowship to F. A.-A. G. L. was supported by a Marie Curie International Outgoing Fellowship within the 7th European Community Framework Programme. D.L.M. is an AHA Established Investigator.

## References

1. Catterall WA. From ionic currents to molecular mechanisms: the structure and function of voltage-gated sodium channels. Neuron. 2000; 26:13–25. [PubMed: 10798388]
2. Hille, B. Ion Channels of Excitable Membranes. 3rd edit. Sunderland, MA: Sinauer Associates, Inc; 2001.
3. Mantegazza M, Curia G, Biagini G, Ragsdale DS, Avoli M. Voltagegated sodium channels as therapeutic targets in epilepsy and other neurological disorders. Lancet Neurol. 2010; 9:413–424. [PubMed: 20298965]
4. Bhattacharya A, Wickenden AD, Chaplan SR. Sodium channel blockers for the treatment of neuropathic pain. Neurotherapeutics. 2009; 6:663–678. [PubMed: 19789071]

5. Etheridge SM. Paralytic shellfish poisoning: seafood safety and human health perspectives. Toxicon. 2010; 56:108–122. [PubMed: 20035780]
6. Yu FH, Catterall WA. The VGL-chanome: a protein superfamily specialized for electrical signaling and ionic homeostasis. Sci STKE. 2004; 2004 re15.
7. Yu FH, Yarov-Yarovoy V, Gutman GA, Catterall WA. Overview of molecular relationships in the voltage-gated ion channel superfamily. Pharmacol Rev. 2005; 57:387–395. [PubMed: 16382097]
8. Heinemann SH, Terlau H, Stuhmer W, Imoto K, Numa S. Calcium channel characteristics conferred on the sodium channel by single mutations. Nature. 1992; 356:441–443. [PubMed: 1313551]
9. Favre I, Moczydlowski E, Schild L. On the structural basis for ionic selectivity among Na+, K+, and Ca2+ in the voltage-gated sodium channel. Biophys J. 1996; 71:3110–3125. [PubMed: 8968582]
10. Tang S, Mikala G, Bahinski A, Yatani A, Varadi G, Schwartz A. Molecular localization of ion selectivity sites within the pore of a human L-type cardiac calcium channel. J Biol Chem. 1993; 268:13026–13029. [PubMed: 8099908]
11. Ren D, Navarro B, Xu H, Yue L, Shi Q, Clapham DE. A prokaryotic voltage-gated sodium channel. Science. 2001; 294:2372–2375. [PubMed: 11743207]
12. Koishi R, Xu H, Ren D, Navarro B, Spiller BW, Shi Q, Clapham DE. A superfamily of voltage-gated sodium channels in bacteria. J Biol Chem. 2004; 279:9532–9538. [PubMed: 14665618]
13. Irie K, Kitagawa K, Nagura H, Imai T, Shimomura T, Fujiyoshi Y. Comparative study of the gating motif and C-type inactivation in prokaryotic voltagegated sodium channels. J Biol Chem. 2010; 285:3685–3694. [PubMed: 19959480]
14. Charalambous K, Wallace BA. NaChBac: the long lost sodium channel ancestor. Biochemistry. 2011; 50:6742–6752. [PubMed: 21770445]
15. Payandeh J, Scheuer T, Zheng N, Catterall WA. The crystal structure of a voltage-gated sodium channel. Nature. 2011; 475:353–358. [PubMed: 21743477]
16. Payandeh J, Gamal El-Din TM, Scheuer T, Zheng N, Catterall WA. Crystal structure of a voltage-gated sodium channel in two potentially inactivated states. Nature. 2012; 486:135–139. [PubMed: 22678296]
17. Zhang X, Ren W, DeCaen P, Yan C, Tao X, Tang L, Wang J, Hasegawa K, Kumasaka T, He J, Clapham DE, Yan N. Crystal structure of an orthologue of the NaChBac voltage-gated sodium channel. Nature. 2012; 486:130–134. [PubMed: 22678295]
18. McCusker EC, D'Avanzo N, Nichols CG, Wallace BA. A simplified bacterial "Pore" provides insight into the assembly, stability and structure of sodium channels. J Biol Chem. 2011; 286:16386–16391. [PubMed: 21454659]
19. Shaya D, Kreir M, Robbins RA, Wong S, Hammon J, Bruggemann A, Minor DL Jr. Voltage-gated sodium channel (NaV) protein dissection creates a set of functional pore-only proteins. Proc Natl Acad Sci U S A. 2011; 108:12313–12318. [PubMed: 21746903]
20. McCusker EC, Bagneris C, Naylor CE, Cole AR, D'Avanzo N, Nichols CG, Wallace BA. Structure of a bacterial voltage-gated sodium channel pore reveals mechanisms of opening and closing. Nat Commun. 2012; 3:1102. [PubMed: 23033078]
21. Caprini M, Ferroni S, Planells-Cases R, Rueda J, Rapisarda C, Ferrer-Montiel A, Montal M. Structural compatibility between the putative voltage sensor of voltage-gated K+ channels and the prokaryotic KcsA channel. J Biol Chem. 2001; 276:21070–21076. [PubMed: 11274182]
22. Lu Z, Klem AM, Ramu Y. Ion conduction pore is conserved among potassium channels. Nature. 2001; 413:809–813. [PubMed: 11677598]
23. Lu Z, Klem AM, Ramu Y. Coupling between voltage sensors and activation gate in voltage-gated K+ channels. J Gen Physiol. 2002; 120:663–676. [PubMed: 12407078]
24. Arrigoni C, Schroeder I, Romani G, Van Etten JL, Thiel G, Moroni A. The voltage-sensing domain of a phosphatase gates the pore of a potassium channel. J Gen Physiol. 2013; 141:389–395. [PubMed: 23440279]
25. Long SB, Campbell EB, Mackinnon R. Crystal structure of a mammalian voltage-dependent Shaker family K+ channel. Science. 2005; 309:897–903. [PubMed: 16002581]
26. Long SB, Tao X, Campbell EB, MacKinnon R. Atomic structure of a voltage-dependent K+ channel in a lipid membrane-like environment. Nature. 2007; 450:376–382. [PubMed: 18004376]

27. Jiang Y, Lee A, Chen J, Ruta V, Cadene M, Chait BT, MacKinnon R. X-ray structure of a voltage-dependent K+ channel. Nature. 2003; 423:33–41. [PubMed: 12721618]
28. Powl AM, O'Reilly AO, Miles AJ, Wallace BA. Synchrotron radiation circular dichroism spectroscopy-defined structure of the C-terminal domain of NaChBac and its role in channel assembly. Proc Natl Acad Sci U S A. 2010; 107:14064–14069. [PubMed: 20663949]
29. Irie K, Shimomura T, Fujiyoshi Y. The C-terminal helical bundle of the tetrameric prokaryotic sodium channel accelerates the inactivation rate. Nat Commun. 2012; 3:793. [PubMed: 22531178]
30. Mio K, Mio M, Arisaka F, Sato M, Sato C. The C-terminal coiled-coil of the bacterial voltage-gated sodium channel NaChBac is not essential for tetramer formation, but stabilizes subunit-to-subunit interactions. Prog Biophys Mol Biol. 2010; 103:111–121. [PubMed: 20678983]
31. Begenisich T. Molecular properties of ion permeation through sodium channels. Annu Rev Biophys Biophys Chem. 1987; 16:247–263. [PubMed: 2439097]
32. Tsien RW, Hess P, McCleskey EW, Rosenberg RL. Calcium channels: mechanisms of selectivity, permeation, and block. Annu Rev Biophys Biophys Chem. 1987; 16:265–290. [PubMed: 2439098]
33. Yang J, Ellinor PT, Sather WA, Zhang JF, Tsien RW. Molecular determinants of Ca2+ selectivity and ion permeation in L-type Ca2+ channels. Nature. 1993; 366:158–161. [PubMed: 8232554]
34. Hess P, Tsien RW. Mechanism of ion permeation through calcium channels. Nature. 1984; 309:453–456. [PubMed: 6328315]
35. Zhang X, Xia M, Li Y, Liu H, Jiang X, Ren W, Wu J, DeCaen P, Yu F, Huang S, He J, Clapham DE, Yan N, Gong H. Analysis of the selectivity filter of the voltage-gated sodium channel Na(v)Rh. Cell Res. 2012; 23:409–422. [PubMed: 23247626]
36. Carnevale V, Treptow W, Klein ML. Sodium Ion Binding Sites and Hydration in the Lumen of a Bacterial Ion Channel from Molecular Dynamics Simulations. Journal of Physical Chemistry Letters. 2011; 2:2504–2508.
37. Karplus PA, Diederichs K. Linking crystallographic model and data quality. Science. 2012; 336:1030–1033. [PubMed: 22628654]
38. Evans PR, Murshudov GN. How good are my data and what is the resolution? Acta Crystallogr D Biol Crystallogr. 2013; 69:1204–1214. [PubMed: 23793146]
39. Diederichs K, Karplus PA. Better models by discarding data? Acta Crystallogr D Biol Crystallogr. 2013; 69:1215–1222. [PubMed: 23793147]
40. Uysal S, Vasquez V, Tereshko V, Esaki K, Fellouse FA, Sidhu SS, Koide S, Perozo E, Kossiakoff A. Crystal structure of full-length KcsA in its closed conformation. Proc Natl Acad Sci U S A. 2009; 106:6644–6649. [PubMed: 19346472]
41. Howard RJ, Clark KA, Holton JM, Minor DL Jr. Structural insight into KCNQ (Kv7) channel assembly and channelopathy. Neuron. 2007; 53:663–675. [PubMed: 17329207]
42. Wiener R, Haitin Y, Shamgar L, Fernandez-Alonso MC, Martos A, Chomsky-Hecht O, Rivas G, Attali B, Hirsch JA. The KCNQ1 (Kv7.1) COOH terminus, a multitiered scaffold for subunit assembly and protein interaction. J Biol Chem. 2008; 283:5815–5830. [PubMed: 18165683]
43. Tsuruda PR, Julius D, Minor DL Jr. Coiled coils direct assembly of a cold-activated TRP channel. Neuron. 2006; 51:201–212. [PubMed: 16846855]
44. Lomize MA, Lomize AL, Pogozheva ID, Mosberg HI. OPM: orientations of proteins in membranes database. Bioinformatics. 2006; 22:623–625. [PubMed: 16397007]
45. Pidcock E, Moore GR. Structural characteristics of protein binding sites for calcium and lanthanide ions. J Biol Inorg Chem. 2001; 6:479–489. [PubMed: 11472012]
46. Zheng H, Chruszcz M, Lasota P, Lebioda L, Minor W. Data mining of metal ion environments present in protein structures. J Inorg Biochem. 2008; 102:1765–1776. [PubMed: 18614239]
47. Yue L, Navarro B, Ren D, Ramos A, Clapham DE. The cation selectivity filter of the bacterial sodium channel, NaChBac. J Gen Physiol. 2002; 120:845–853. [PubMed: 12451053]
48. Parent L, Gopalakrishnan M. Glutamate substitution in repeat IV alters divalent and monovalent cation permeation in the heart Ca2+ channel. Biophys J. 1995; 69:1801–1813. [PubMed: 8580323]
49. Findeisen F, Minor DL Jr. Disruption of the IS6-AID Linker Affects Voltagegated Calcium Channel Inactivation and Facilitation. J Gen Physiol. 2009; 133:327–343. [PubMed: 19237593]

50. Bagriantsev SN, Clark KA, Minor DL Jr. Metabolic and thermal stimuli control K(2P)2.1 (TREK-1) through modular sensory and gating domains. EMBO J. 2012; 31:3297–3308. [PubMed: 22728824]
51. O'Neil KT, DeGrado WF. A thermodynamic scale for the helix-forming tendencies of the commonly occurring amino acids. Science. 1990; 250:646–651. [PubMed: 2237415]
52. Doyle DA, Morais Cabral J, Pfuetzner RA, Kuo A, Gulbis JM, Cohen SL, Chait BT, MacKinnon R. The structure of the potassium channel: molecular basis of $K^+$ conduction and selectivity. Science. 1998; 280:69–77. [PubMed: 9525859]
53. Xu Q, Chang A, Tolia A, Minor DL Jr. Structure of a Ca(2+)/CaM:Kv7.4 (KCNQ4) B-helix complex provides insight into M current modulation. J Mol Biol. 2013; 425:378–394. [PubMed: 23178170]
54. Haitin Y, Attali B. The C-terminus of Kv7 channels: a multifunctional module. J Physiol. 2008; 586:1803–1810. [PubMed: 18218681]
55. Pavlov E, Bladen C, Winkfein R, Diao C, Dhaliwal P, French RJ. The pore, not cytoplasmic domains, underlies inactivation in a prokaryotic sodium channel. Biophys J. 2005; 89:232–242. [PubMed: 15849254]
56. Zhou Y, Morais-Cabral JH, Kaufman A, MacKinnon R. Chemistry of ion coordination and hydration revealed by a K+ channel-Fab complex at 2.0 A resolution. Nature. 2001; 414:43–48. [PubMed: 11689936]
57. Chakrabarti N, Ing C, Payandeh J, Zheng N, Catterall WA, Pomes R. Catalysis of Na+ permeation in the bacterial sodium channel NaVAb. Proc Natl Acad Sci U S A. 2013; 110:11331–11336. [PubMed: 23803856]
58. Jiang J, Lafer EM, Sousa R. Crystallization of a functionally intact Hsc70 chaperone. Acta Crystallogr Sect F Struct Biol Cryst Commun. 2006; 62:39–43.
59. Clarke OB, Caputo AT, Hill AP, Vandenberg JI, Smith BJ, Gulbis JM. Domain reorientation and rotation of an intracellular assembly regulate conduction in Kir potassium channels. Cell. 2010; 141:1018–1029. [PubMed: 20564790]
60. Leslie AGW. Recent changes to the MOSFLM package for processing film and image plate data. Joint CCP4 + ESF-EAMCB Newsletter of Protein Crystallography. 1992; 26
61. Evans PR. An introduction to data reduction: space-group determination, scaling and intensity statistics. Acta Crystallogr D Biol Crystallogr. 2011; 67:282–292. [PubMed: 21460446]
62. McCoy AJ, Grosse-Kunstleve RW, Adams PD, Winn MD, Storoni LC, Read RJ. Phaser crystallographic software. J Appl Crystallogr. 2007; 40:658–674. [PubMed: 19461840]
63. Emsley P, Cowtan K. Coot: model-building tools for molecular graphics. Acta Crystallogr D Biol Crystallogr. 2004; 60:2126–2132. [PubMed: 15572765]
64. Collaborative Computational Project N. The CCP4 suite: Programs for protein crystallography. Acta Crystallogr D Biol Crystallogr. 1994; 50:760–763. [PubMed: 15299374]
65. Hamill OP, Marty A, Neher E, Sakmann B, Sigworth FJ. Improved patch-clamp techniques for high-resolution current recording from cells and cell-free membrane patches. Pflugers Arch. 1981; 391:85–100. [PubMed: 6270629]
66. Chovancova E, Pavelka A, Benes P, Strnad O, Brezovsky J, Kozlikova B, Gora A, Sustr V, Klvana M, Medek P, Biedermannova L, Sochor J, Damborsky J. CAVER 3.0: a tool for the analysis of transport pathways in dynamic protein structures. PLoS Comput Biol. 2012; 8:e1002708. [PubMed: 23093919]

## Highlights

- Bacterial voltage-gated sodium channels (BacNa$_V$s) neck region is involved in gating
- BacNaV neck region undergoes a helix-→disorder transition upon channel opening
- BacNaV selectivity filter has an outer ion binding site
- Outer ion binding site is shared with mammalian voltage-gated calcium channels

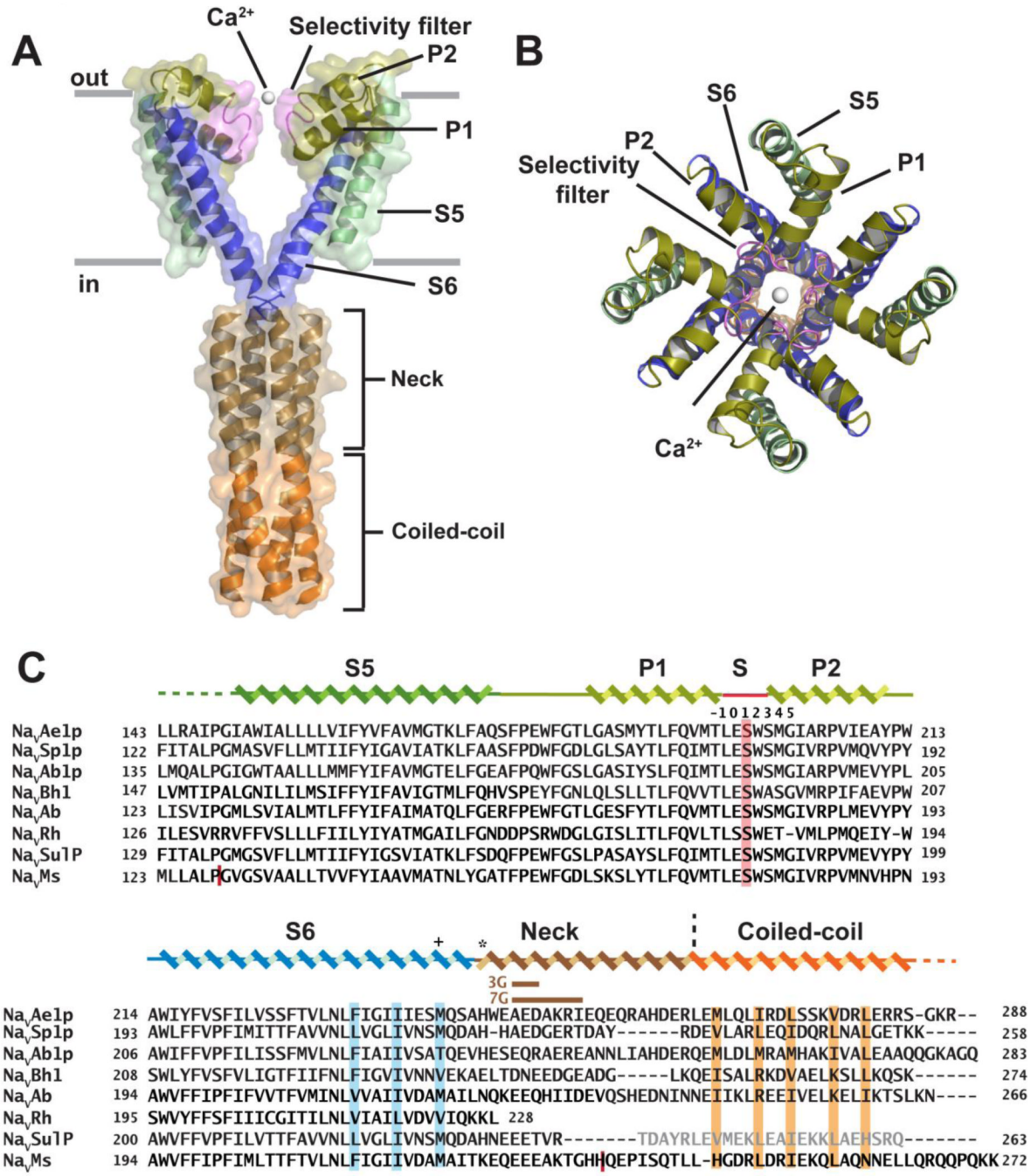


**Figure 1. Structure of the *Alkalilimnicola ehrlichei* pore-only sodium channel protein $Na_VAe1p$**

**A**, Side view showing two transmembrane region subunits and four cytoplasmic tail subunits. Transmembrane helices S5 and S6 are colored in green and blue, respectively. P1 and P2 pore-helices are colored in olive. Selectivity filter is violet. Neck and coiled-coil are tan and orange, respectively. Calcium ion is a white sphere. Grey lines show approximate lipid bilayer boundaries. **B**, $Na_VAe1p$ tetramer extracellular view. Colors are as in 'A'. **C**, $Na_VAe1p$ secondary structure and alignment with $BacNa_V$ pore domain sequences. $Na_VAe1p$ secondary structure elements are indicated and colored as in 'A'. Selectivity filter position numbers are indicated relative to position '0', $Na_VAe1p$ Glu197. '+' indicates the

activation gate residue. '*' indicates position of the $Na_VAe1p$ His245 bend. Vertical black dashed line indicates division between 'Neck' and 'Coiled-coil'. Colored bars indicate: selectivity filter (+1) position, red; S6 pore lining, blue; and coiled-coil core residues, orange. Positions of 3Gly and 7Gly neck mutants are indicated in brown. Grey letters show $Na_VSulP$ portion used in the NaK chimera [29]. Red vertical lines show crystallized $Na_VMs$ pore-only construct boundaries [20]. Other sequences are: $Na_VSp1p$, *Silicibacter pomeroyi* [19]; $Na_VAb1p$, *Alcanivorax borkumensis* [19]; $Na_VBh1$ (NaChBac), *Bacillus halodurans* [11]; $Na_VAb$ *Acrobacter butzleri* (GI 157737984)[15]; $Na_VRh$, *Rickettsiales sp*. (GI: 262276647)[15], $Na_VSulP$ *Sulfitobacter pontiacus* (GI ZP_00961826.1)[29]; and $Na_VMs$, *Magnetococcus sp*. (Uniprot ID A0L5S6)[20].

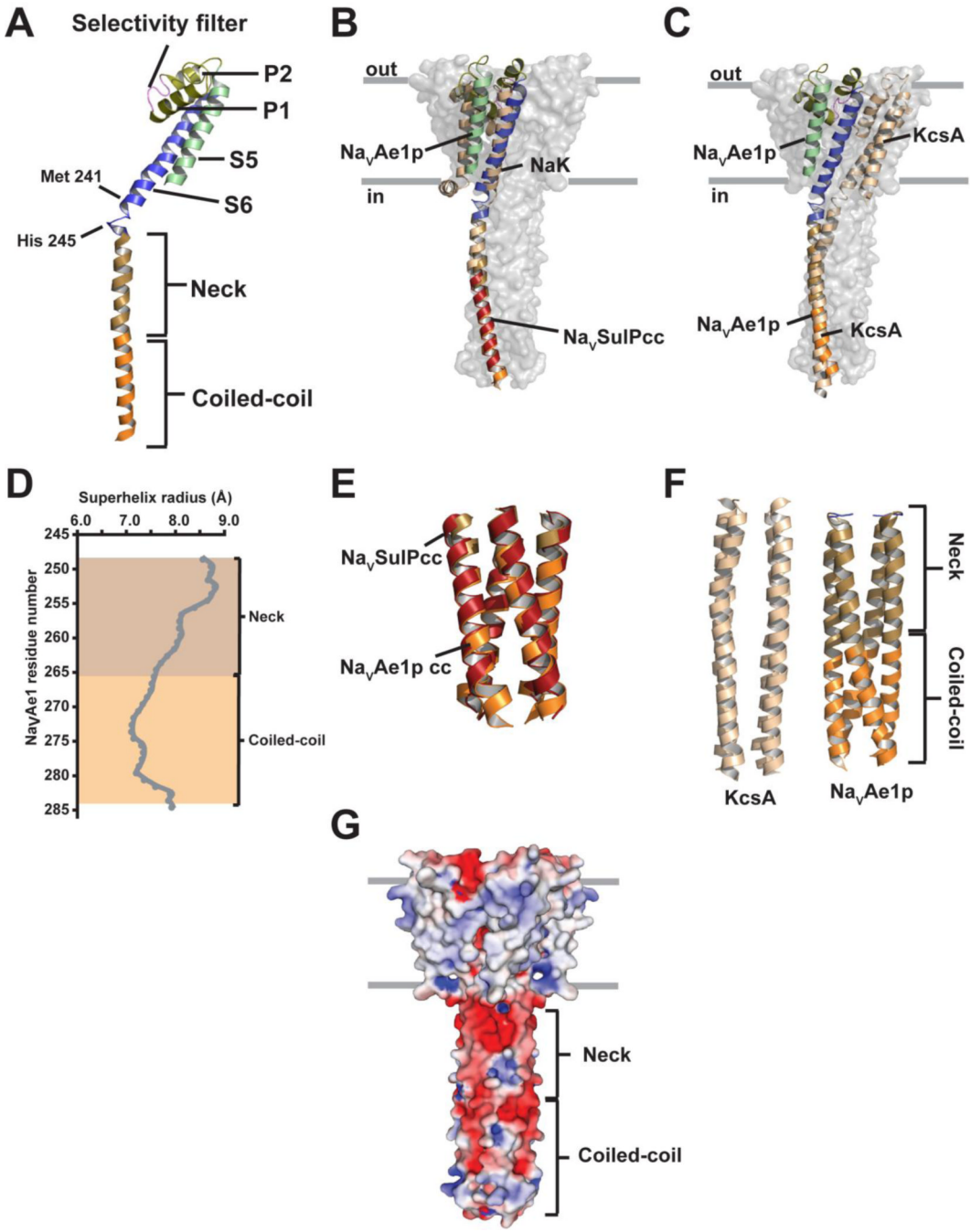


**Figure 2. $Na_VAe1p$ structure comparison and analysis**

**A**, Side view of a single $Na_VAe1p$ monomer. Secondary structure elements are labeled and colored as in Figure 1. Select residue positions are indicated. **B**, Cα superposition of the tetrameric $Na_VSulP$ region of the NaK-NaVSulP chimera [29] ($Na_VSulP$ portion, red; NaK portion, wheat) with equivalent parts of the $Na_VAe1p$ neck and coiled-coil (colored as in Figure 1). One $Na_VAe1p$ and NaK-$Na_VSulP$ chimera monomer is shown in cartoon representation in front of the surface of three remaining $Na_VAe1p$ subunits. **C**, Cα superposition of the $Na_VAe1p$ coiled-coil tetramer with the equivalent KcsA residues. One $Na_VAe1p$ (colored as in Fig. 1) and KcsA (wheat) monomer is shown in cartoon

representation in front of the surface of three remaining $Na_VAe1p$ subunits. **D**, Plot of $Na_VAe1p$ coiled-coil superhelix radius versus residue number. Neck and coiled-coil elements are shaded as in 'A. **E**, Close-up of the coiled-coil regions of $Na_VAe1p$ (orange) and $Na_VSulP$ (red) used for superposition in **'B'. F**, Close-up of the cytoplasmic parts of KcsA (left panel, wheat) and $Na_VAe1p$ (neck, sand; coiled-coil, orange). **G**, $Na_VAe1p$ electrostatic surface potential (+4kT (blue) to −4kT (red)) mapped on the channel van der Waals surface. Grey lines show approximate lipid bilayer boundaries.

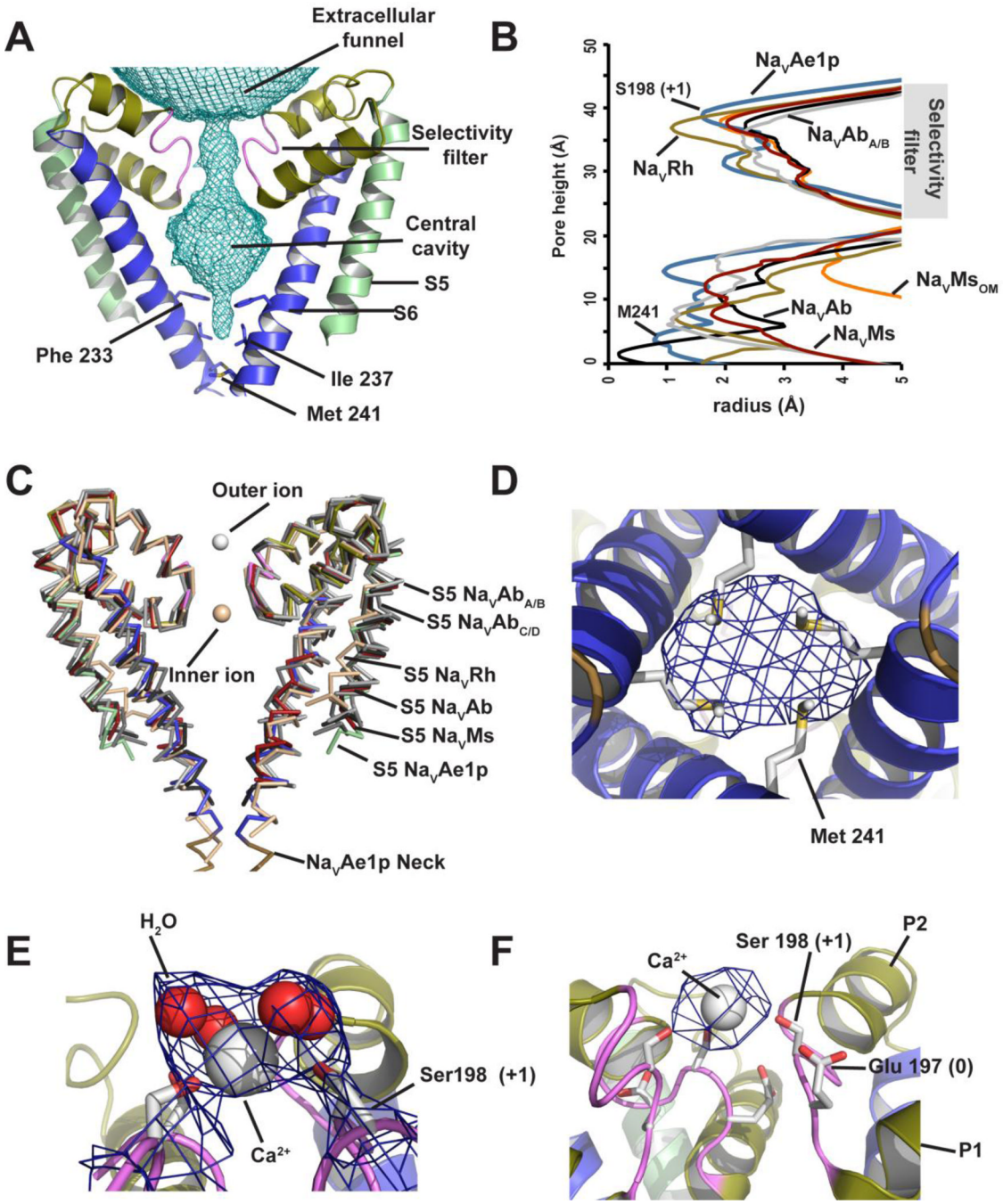


**Figure 3. $Na_VAe1p$ pore region analysis**

**A**, $Na_VAe1p$ Pore volume represented as a teal mesh calculated by CAVER [66]. In order to show the central cavity, dummy atoms closed the side vestibules. S6 residues forming the narrow constriction are shown as sticks and labeled. $Na_VAe1p$ elements are labeled as in Figure 1. **B**, Plot of channel radius versus distance along the central channel axis for closed $Na_VAb$ [15] (black), inactivated $Na_VAbA/_B$ [16] (light grey), $Na_VRh$ [15] (wheat), $Na_VMs$ (dark red) [20], $Na_VMs_OM$ (orange) open state model following [20], and $Na_VAe1p$ (blue). $Na_VAe1p$ constriction points caused by selectivity filter residue Ser198 and S6 residue Met241 are indicated. **C**, Backbone superposition of PDs of $Na_VAb$ [15] (black), NaVAbA/B [16] (light

grey), $Na_VAb_{C/D}$ [16] (medium grey), $Na_VRh$ [17] (wheat), $Na_VMs$ [20] (dark red), and $Na_VAe1p$ (colored as in 'A'). Outer ion from $Na_VAe1p$ and inner ion from $Na_VRh$ are shown as white and wheat spheres, respectively. Two subunits are shown. **D**, View from the intracellular side showing M241 sidechain Fo-Fc density. **E**, Outer ion site side view. $Ca^{2+}$ (white sphere) is surrounded by four water molecules (red spheres), and Ser198 (+1) shown in sticks with $2F_O$-$F_C$ density surrounding the $Ca^{2+}$ ion as a 1.0σ contoured blue mesh. **F**, Side view of outer ion anomalous difference density (blue mesh) calculated at 6.5 Å and contoured at 6.5σ. Glu197 (0) and Ser198 (+1) are indicated. $Ca^{2+}$ is shown as a white sphere. The front channel monomer is removed for clarity.

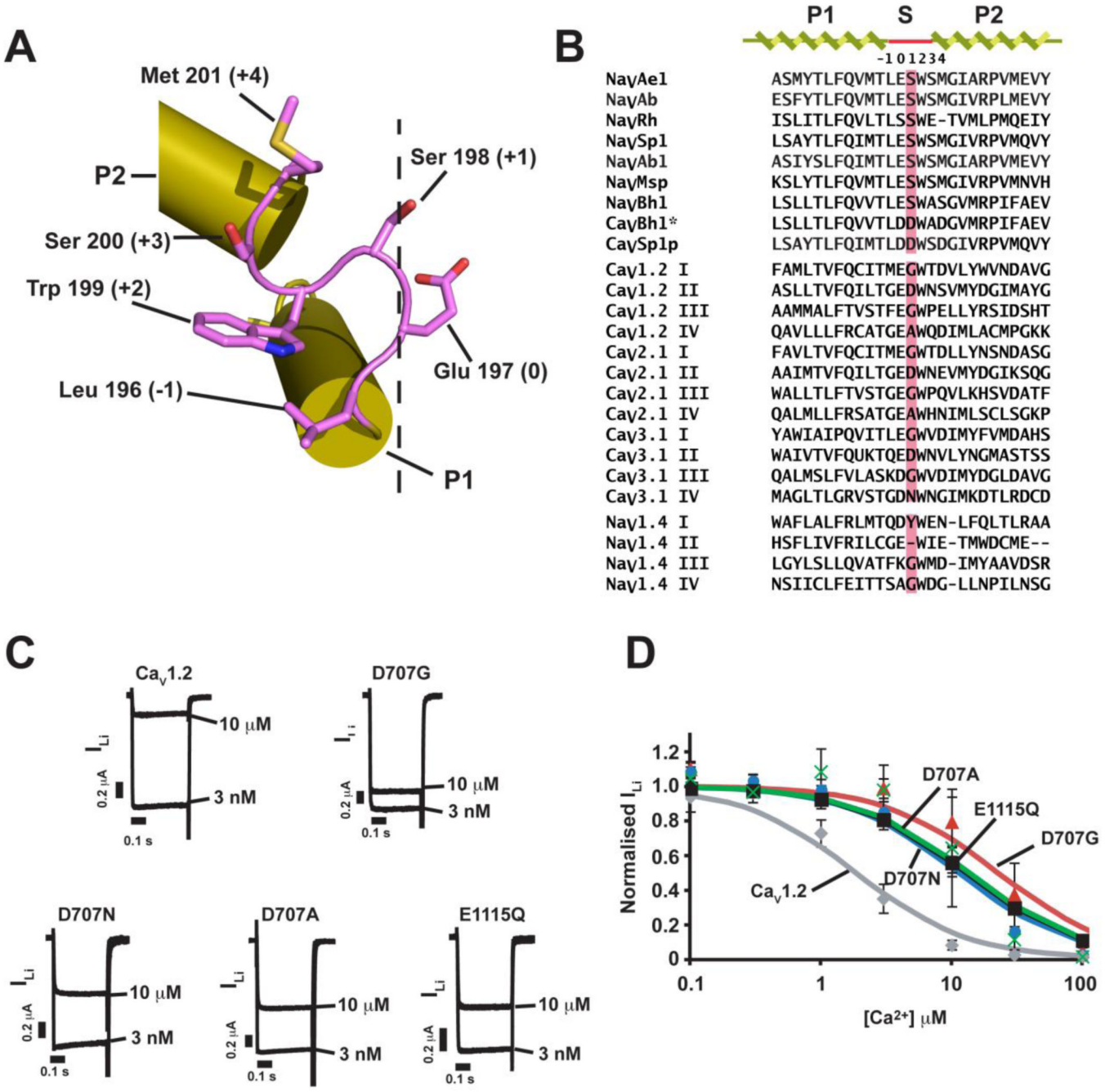


**Figure 4. Selectivity filter (+1) position is conserved in mammalian $Ca_V$s and important for ion binding**

**A**, Cartoon depiction of a single $Na_V$Ae1p subunit selectivity filter colored as in Figure 1. Selectivity filter residues are shown and indicated relative to the (0) position glutamate. Dashed line shows the central pore axis approximate position. **B**, Selectivity filter and pore helices sequence alignment for selected Bac$Na_V$s, mammalian $Ca_V$ subtype exemplars, and mammalian $Na_V$1.4. $Ca_V$Bh1 and $Ca_V$Sp1p are calcium selective mutants of $Na_V$Bh1 (NaChBac) [47] and $Na_V$Sp1p [19] respectively. Selectivity filter numbering is indicated. **C**, Two-electrode voltage-clamp recordings from *Xenopus* oocyte expressing wild-type $Ca_V$1.2 or the indicated mutants recorded in a buffer containing 100 mM $Li^+$ and either 3 nM or 10

μM free $Ca^{2+}$ and normalized to the 3 nM trace. Currents were elicited by a voltage step from −90 mV to −20 mV. **D**, Dose-response curves for calcium block of lithium currents for $Ca_V1.2$ (grey), E1115Q (black), D707N (blue), D707A (green), and D707G (red). Each data point at each calcium concentration is normalized to the current at 3 nM $Ca^{2+}$ and averaged for n = 5–7 oocytes. Error bars are s.e.m.

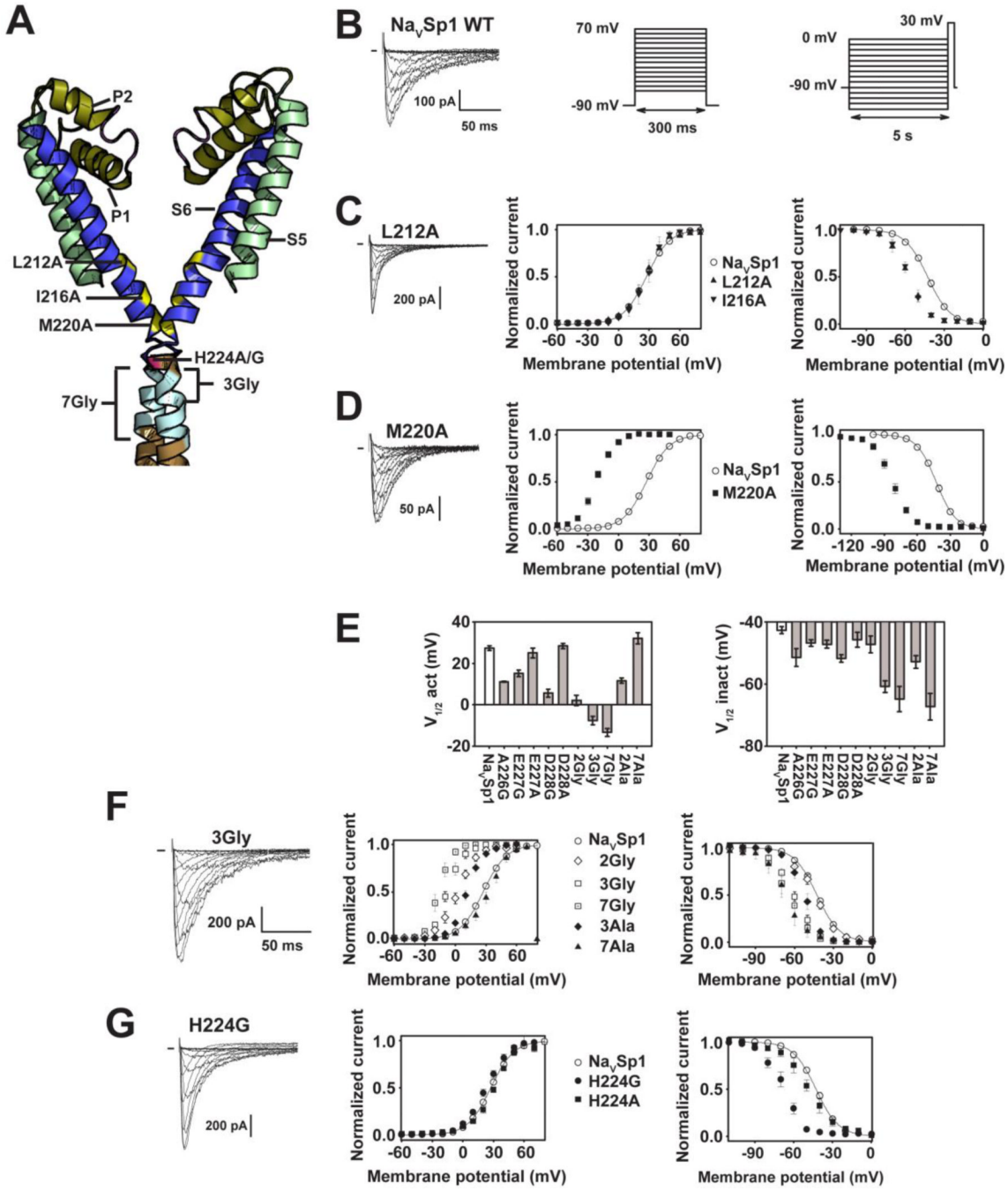


**Figure 5. Functional studies of $Na_VSp1$ structure-based mutants**

**A**, $Na_VAe1p$ cartoon depicting positions investigated by patch-clamp. S6, bend, and neck positions are colored yellow, red, and light blue, respectively and indicated using the corresponding $Na_VSp1$ residues. **B**, Left panel, exemplar $Na_VSp1$ $Na^+$ currents in response to the activation protocol shown in the middle panel (300 ms depolarizations to −60 to +70 mV in 10 mV steps from a holding potential of −90 mV, sweep to sweep interval = 10 s). Right panel, protocol for examining steady state inactivation voltage dependence (5 s pre-pulse depolarization from 0 to −130 mV in 10 mV steps, followed by a 300 ms step to +30 mV, and repolarization to the holding potential, −90 mV. Sweep to sweep interval = 5 s). **C**,

Left panel, exemplar $Na_VSp1$ L212A $Na^+$ currents. Activation (middle panel) and inactivation curves (right panel) of: $Na_VSp1$ (open circles), L212A (black triangle) and I216A (inverted black triangle). **D**, Left panel, exemplar $Na_VSp1$ M220A $Na^+$ currents. Activation (middle panel) and inactivation curves (right panel) of: $Na_VSp1$ (open circles) and M220A (black squares). **E**, $V_{1/2}$ act and $V_{1/2}$ inact for $Na_VSp1$ and indicated neck mutants. **F**, Left panel, exemplar $Na_VSp1$ 3Gly $Na^+$ currents. Activation (middle panel) and inactivation curves (right panel) of: $Na_VSp1$ (open circles), 2Gly (open diamonds), 3Gly (open squares), 7Gly (filled open squares), 3Ala (black diamonds), and 7Ala (black triangles). **G**, Left panel, exemplar $Na_VSp1$ H224G $Na^+$ currents. Activation (middle panel) and inactivation curve (right panel) of: NavSp1 (open circles), H224G (black circles), and H224A (black squares). Activation curves are obtained by normalizing maximal amplitudes divided by the driving force. Inactivation curves are obtained by normalizing maximum amplitudes upon second pulse. NavSp1 activation and inactivation curve Boltzmann fits are shown in '**C**', '**D**', '**F**', and '**G**'.

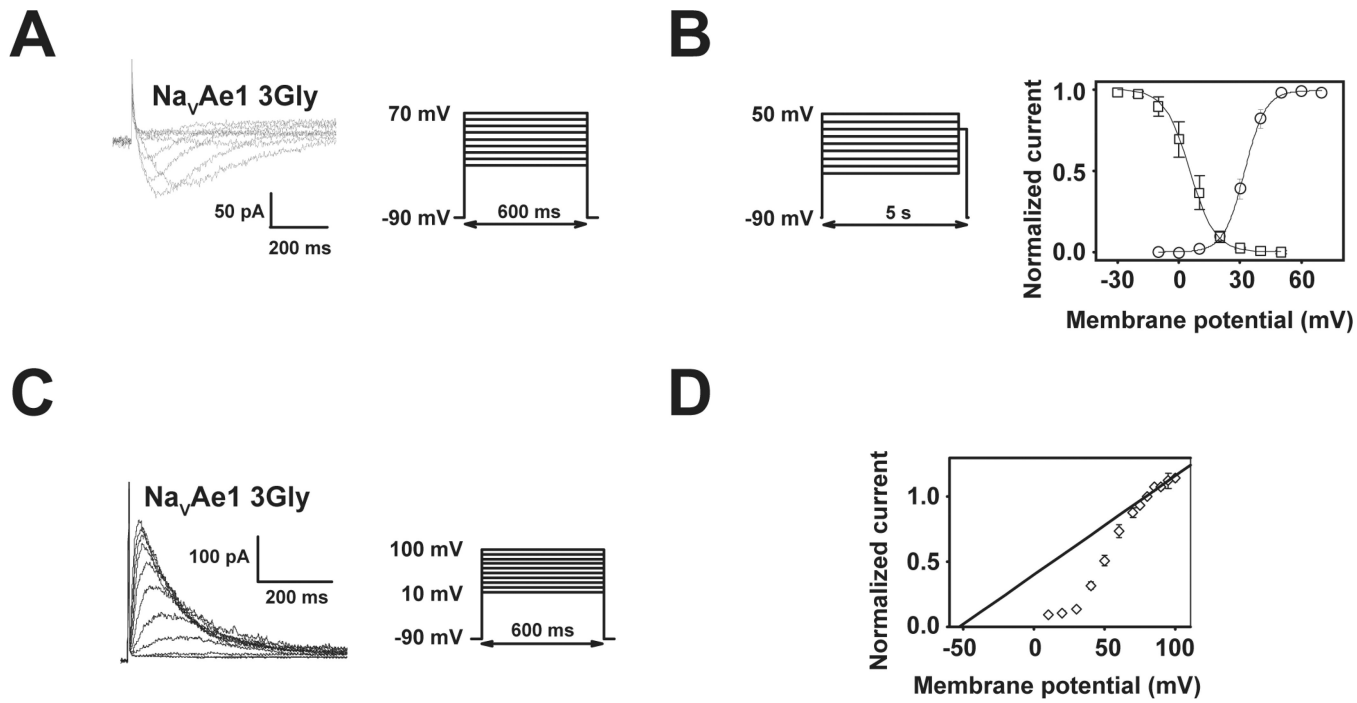


**Figure 6. Na$_V$Ae1 functional properties**

**A**, Left panel, exemplar NavAe1 3Gly $Na^+$ currents in response to an activation protocol, right panel (600 ms depolarizations to 0 to +70 mV in 10 mV steps from a holding potential of −90 mV, sweep to sweep interval = 5 s). **B**, Left panel, protocol for examining steady state inactivation voltage dependence (5 s pre-pulse depolarization from to 50 to −30 mV in 10 mV steps, followed by a 300 ms step to +30 mV, and repolarization to the holding potential, −90 mV. Sweep to sweep interval = 10 s). Right panel, Na$_V$Ae1 3Gly activation and inactivation curves. Boltzmann fits are indicated. **C**, Left panel, exemplar Na$_V$Ae1 3Gly currents in presence of 130 mM intracellular $Na^+$ and 107.5 mM extracellular $Ca^{2+}$, in response to an activation protocol, right panel (600 ms depolarizations to 10 to +100 mV in variable steps (10 mV and then 5 mV after 70 mV) from a holding potential of −90 mV, sweep to sweep interval = 5 s). **D**, Normalized current-voltage curve from '**C**'. Reversal potential can be obtained by linear regression, as indicated. The averaged value obtained by this method (n=5) gives $E_{rev}$ = −52.1 ± 10.3 mV, which corresponds to $P_{Ca}/P_{Na}$ = 0.07 ± 0.02 (n=5) when corrected for the liquid junction potential (-17mV).

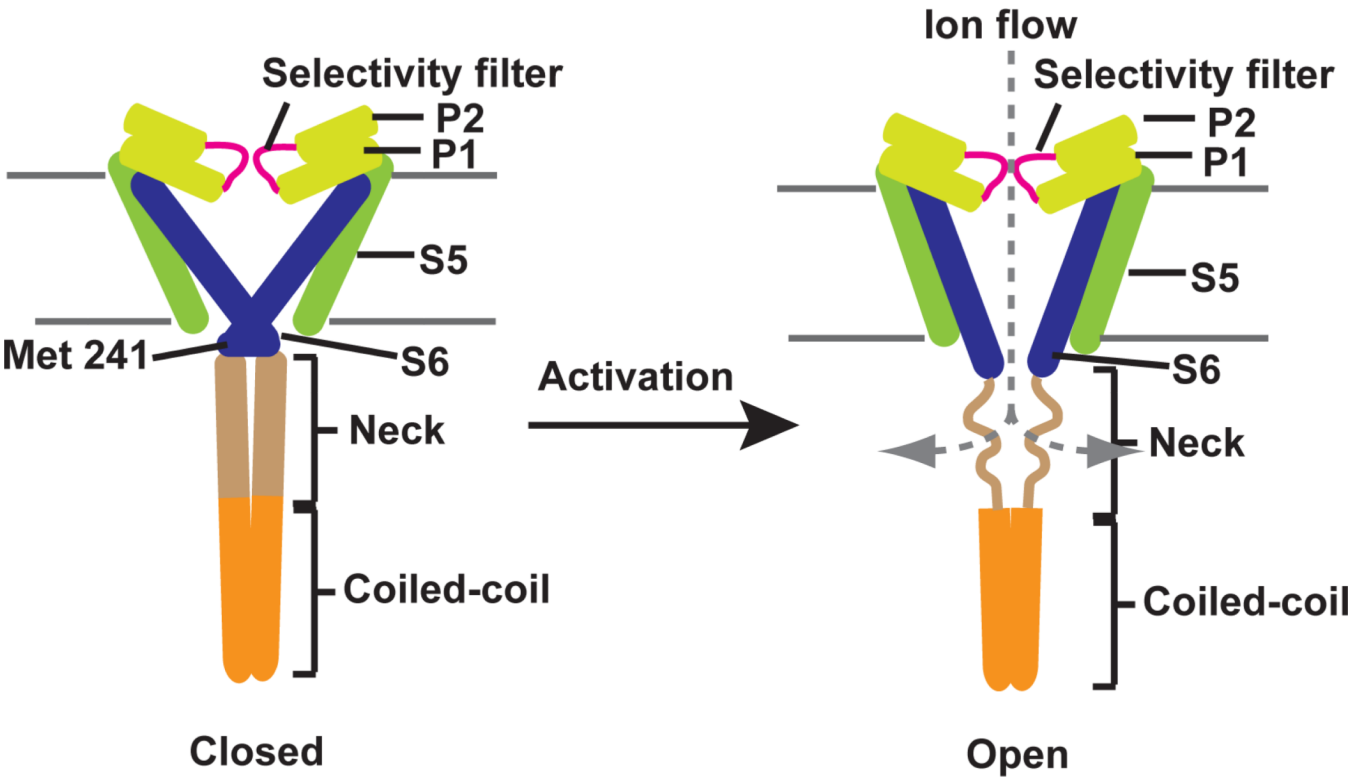


**Figure 7. Cartoon model of BacNa$_V$ gating**

Activation of BacNa$_V$s is proposed to involve the expansion of the pore at the activation gate (Met 241) and an order→disorder transition in the neck region. Ions can escape into the cytoplasm through spaces created by the neck region. Channel elements are colored as in Figure 1. VSDs are not shown.

**Table 1**

Activation and inactivation properties of BacNa$_V$s and mutants

| | $V_{1/2, act}$ | $\Delta V_{1/2, act}$ | n | P-Value | V1/2, inact | $\Delta V_{1/2, inact}$ | n | P-Value |
|---|---|---|---|---|---|---|---|---|
| **Na$_V$Sp1** | 27.4 ± 1.1 | − | 13 | n.a. | −42.7 ± 1.1 | − | 12 | n.a. |
| **S6** | | | | | | | | |
| L212A | 26.4 ± 3.1 | −1.0 ± 4.5 | 5 | n.s. | −57.5 ± 2.7 | −14.8 ± 4.3 | 6 | *** |
| I216A | 27.0 ± 3.4 | −0.4 ± 4.8 | 3 | n.s. | −56.7 ± 1.6 | −14.0 ± 3.8 | 4 | *** |
| M220A | −22.4 ± 1.6 | −49.8 ± 3.3 | 7 | *** | −82.7 ± 1.8 | −40.0 ± 3.5 | 7 | *** |
| **Bend** | | | | | | | | |
| H224A | 30.2 ± 1.1 | 2.8 ± 4.2 | 3 | n.s. | −48.1 ± 3.5 | −5.4 ± 4.8 | 3 | n.s. |
| H224G | 22.9 ± 1.7 | −4.5 ± 3.9 | 4 | n.s. | −67.7 ± 2.3 | −25.0 ± 4.0 | 4 | *** |
| **Neck** | | | | | | | | |
| A226G | 11.1 ± 0.2 | −16.3 ± 4.2 | 3 | *** | −51.4 ± 2.8 | −8.7 ± 4.3 | 4 | *** |
| E227G | 15.2 ± 1.5 | −12.2 ± 3.3 | 6 | *** | −46.8 ± 1.1 | −4.1 ± 3.6 | 4 | n.s. |
| E227A | 25.1 ± 2.3 | −2.3 ± 4.1 | 4 | n.s. | −47.1 ± 1.3 | −4.4 ± 3.2 | 6 | * |
| D228G | 5.7 ± 1.9 | −21.7 ± 3.9 | 4 | *** | −51.7 ± 1.2 | −9.0 ± 3.6 | 4 | *** |
| D228A | 28.4 ± 1.3 | 1.0 ± 4.3 | 3 | n.s. | −45.7 ± 2.5 | −3.0 ± 4.2 | 4 | n.s. |
| 2G | 2.1 ± 2.4 | −25.3 ± 2.6 | 6 | *** | −47.2 ± 2.6 | −4.5 ± 3.2 | 4 | n.s. |
| 2A | 11.7 ± 1.3 | −15.7 ± 3.4 | 5 | *** | −52.8 ± 2.0 | −10.1 ± 3.9 | 4 | *** |
| 3G | −7.6 ± 2.1 | −35.0 ± 3.8 | 5 | *** | −60.8 ± 1.9 | −18.1 ± 3.6 | 10 | *** |
| 7G | −13.3 ± 1.9 | −40.7 ± 3.9 | 4 | *** | −64.8 ± 4.1 | −22.1 ± 5.2 | 4 | *** |
| 7A | 32.1 ± 2.8 | 4.7 ± 4.4 | 4 | n.s. | −67.3 ± 4.2 | −24.6 ± 5.2 | 4 | *** |
| **Coiled-coil** | | | | | | | | |
| R242E | 7.8 ± 0.8 | −19.6 ± 3.3 | 5 | *** | −44.4 ± 2.5 | −1.7 ± 4.2 | 4 | n.s. |
| **Na$_V$Ae1** | | | | | | | | |
| 3G | 32.1 ± 1.1 | n.a. | 6 | | 5.3 ± 3.1 | | 4 | |

Data are mean ± s.e.m.

$\Delta V_{1/2}$ '±' denotes 90% confidence interval P values are calculated relative to wild-type Na$_V$Sp1 n.s., Not significant, P > 0.05

* indicates 0.001 < P < 0.05

*** indicates, P< 0.001